Biocompatible Direct Deposition of Functionalized Nanoparticles Using Shrinking Surface Plasmonic Bubble

Seunghyun Moon, Qiushi Zhang, Dezhao Huang, Satyajyoti Senapati, Hsueh-Chia Chang, Eungkyu Lee,* and Tengfei Luo*

Functionalized nanoparticles (NPs) are the foundation of diverse applications. Especially, in many biosensing applications, concentrating suspended NPs onto a surface without deteriorating their biofunction is usually an inevitable step to improve detection limit, which remains to be a great challenge. In this work, biocompatible deposition of functionalized NPs to optically transparent surfaces is demonstrated using shrinking bubbles. Leveraging the shrinking phase of bubble mitigates the biomolecule degradation problems encountered in traditional photothermal deposition techniques. The deposited NPs are closely packed, and the functional molecules are able to survive the process as verified by their strong fluorescence signals. Using high-speed videography, it is revealed that the contracting contact line of the shrinking bubble forces the NPs captured by the contact line to a highly concentrated island. Such shrinking surface bubble deposition (SSBD) is low temperature in nature as no heat is added during the process. Using a hairpin DNA-functionalized gold NP suspension as a model system, SSBD is shown to enable much stronger fluorescence signal compared to the optical-pressure deposition and the conventional thermal bubble contact line deposition. The demonstrated SSBD technique capable of directly depositing functionalized NPs may significantly simplify biosensor fabrication and thus benefit a wide range of relevant applications.

1. Introduction

The ability to manipulate nanoparticles (NPs) decorated by functional molecules is important for a wide range of applications, such as photonics,[1] nanocomposites,[2] energy conversion,[3]

and especially biosensors.[4,5] Advanced biosensing techniques, exemplified by quantum dot Förster resonance energy transfer (FRET)[6] and surface enhanced Raman spectroscopy (SERS),[7] are fundamentally based on the interaction between NPs and functional molecules. As point-of-care (POC) assays become increasingly demanded, diagnosis techniques based on miniaturized microfluidic chips[8] with advanced sensors are being developed aimed at analyzing and quantifying small amounts of analytes. For nucleic acid sensors, exponential amplification reactions are usually required to make low target concentration detectable, but they can be incompatible with POC assays due to its time-consuming nature and the requirement of sophisticated laboratory equipment. In addition, such reactions are not applicable to other targets like proteins, ions and lipids.[5] A more generally applicable strategy is to concentrate targets in the analytes and deposit them onto a surface with prefabricated biomarker detectors. Depending on the sensing mechanism of a chip, fabrication processes using expensive equipment such as vacuum deposition, dry/wet etching and lithography may be required, which inevitable impose cost and throughput barriers for large scale applications.[9] It is thus beneficial to directly concentrate and deposit NPs that capture targets in solution onto substrates in a single step for sensing purposes.

Techniques using nanochannels,[10] magnetic nanobeads,[11] evaporative self-assembly[12] and Langmuir-Blodgett films[13] have been explored to concentrate and deposit suspended particles to surfaces, but depositing them precisely to designated locations, which is important for applications like multiplex sensors, are still very challenging. Previous studies show that fluid flow around an photothermally generated surface bubble can be a promising deposition method with precision.[14,15] The phenomena involved in this process have been extensively studied.[14,16–20] Due to light absorption of metallic nanostructures fabricated on a surface, a spatially localized laser beam is capable of heating-up the focal area so much that a vapor bubble can be created[21] and the temperature gradient around the bubble leads to a Marangoni flow.[22–24] Such a flow near the bubble draw NPs in the suspension to the vapor-liquid interface

Dr. S. Moon, Q. Zhang, D. Huang, Prof. H.-C. Chang,
Dr. E. Lee, Prof. T. Luo
Department of Aerospace and Mechanical Engineering
University of Notre Dame
Notre Dame, IN 46556, USA
E-mail: elee18@nd.edu; tluo@nd.edu
Dr. S. Senapati, Prof. H.-C. Chang, Prof. T. Luo
Department of Chemical and Biomolecular Engineering
University of Notre Dame
Notre Dame, IN 46556, USA
Prof. T. Luo
Center for Sustainable Energy of Notre Dame (ND Energy)
University of Notre Dame
Notre Dame, IN 46556, USA

2000597 (1 of 8)

**ADVANCED
SCIENCE NEWS**
www.advancedsciencenews.com

**ADVANCED
MATERIALS
INTERFACES**
www.advmatinterfaces.de

acting as a trap to capture the NPs. The flow eventually pushes the NPs toward the three-phase contact line (TPCL) and thus deposit them on the surface. This photothermal bubble deposition process has been explored to deposit materials like polystyrene beads,[14,17,23] quantum dots[16,18] and noble metal NPs,[19,20,25] in aqueous environments.

Recently, such an approach has been applied to biomarker detection. In this process, high-power lasers (≈O(100) mW) and light-absorbing plasmonic structures are indispensable for the initial generation of the photothermal bubbles. While the water temperature around the photothermal bubbles under laser illumination is moderately high (≈350 K),[18,25] the laser covered area can have much higher temperatures. In addition, the suspended NPs in the solution can experience intense heating and even supercavitation if the laser wavelength is at their surface plasmon resonance (SPR) peak,[26–28] which would detach any functional molecules from the NP surface immediately. Nevertheless, the Marangoni flow and surface tension, especially at the TPCL, of photothermal bubbles have been studied for capturing and depositing biomarkers like DNA,[29] proteins[30] and microbes.[31,32] However, to avoid damaging the biomolecules by the high temperature close to the laser-heated area, the size of the deposited region of biomarkers is usually a few times larger than the laser beam size, reducing the concentration ratio and thus sensing signal strength. The thermal problem involved in the photothermal bubble deposition technique limits its application in direct deposition of NP-based biosensors.

In this work, we demonstrate that photothermal bubble can be made compatible with the direct deposition of biomolecule-functionalized NPs if we leverage the shrinking phase of the bubble by turning off the photo excitation. Using videography analyses, we elucidate that contracting contact lines of a shrinking bubble force the NPs captured at the TPCL to a highly concentrated island with sizes as small as 3 μm. The concentrated NPs are closely packed, and the functional molecules are able to survive the process. Such a shrinking surface bubble deposition (SSBD) technique is low temperature in nature as no heat is added during the process. Using a hairpin DNA-functionalized gold (Au) NP suspension as a model system, SSBD is shown to enable strong fluorescence signal from the deposited NP island on the surface when reporters are added. We have also compared its performance to that from another two deposition mechanisms, including the optical pressure deposition and the conventional steady state thermal bubble-induced TPCL deposition. It is found the deposited NPs by optical pressure would damage the functional molecules and show no fluorescence signal when reporters are added. The TPCL deposition can still enable fluorescence detection but the signal strength is notably weaker as the deposited NPs spread over a much larger area (>30 μm). Through further experiments, we have also revealed the correlation between the deposited spot size, bubble size and NP concentration in the SSBD process, which is important to its real applications. The SSBD technique demonstrated and physics revealed from this study may benefit a wide range of biosensing applications for scenarios like early detection of epidemic/pandemic infectious disease, cancers and chemical/biological weapons.

2. Results and Discussion

2.1. Mechanism of SSBD

When a laser beam is directed into a AuNP suspension, the optical pressure will drive the irradiated NPs toward the surface (**Figure 1**a) as we elucidated in a recent study.[28] These deposited NPs then act as surface heaters as they continue to convert optical energy into thermal energy, and in the meantime, they are working as nucleation sites for surface bubble nucleation (Figure 1a). In our case, the time delay between laser irradiation and bubble nucleation is found to be ≈1 s when using a laser power density of ≈8.8 mW μm^{-2} at the focal plane, which overlaps with the surface of the substrate. It is because of this optical pressure-driven NP deposition that allows us to generate surface bubble without the need of prefabricated light absorbers[25] as employed in many other studies.[14,16–20,31,33,34] We note that our laser has a wavelength of 800 nm, which matches the SPR peak of the AuNP used in our experiment (see Method section for more experimental details). With the continued heating of the surface NPs, the surface bubble grows due to both water vaporization and dissolved gas diffusion into the cavity (Figure 1b).[35,36]

Particle movement and trapping around a photothermal plasmonic bubble are known to be associated with factors like thermophoresis and convective flow.[14,17,19] Particularly, the laser-illuminated volume above the bubble is hotter than the bottom due to plasmonic heating of the suspended AuNP (Figure S1, Supporting Information).[25] Surface tension gradient along the bubble surface due to such a temperature gradient leads to a Marangoni flow around the bubble (Figure 1b).[23,37] This flow exerts drag force on the suspended AuNPs and carry them toward the bubble surface. When the NPs are brought to the close proximity of the bubble, the competition between the surface tension and pressure difference captures and traps the NPs at the bubble surface. The force due to surface tension pulls the NPs toward the center of the bubble, while the force caused by the pressure difference at the bubble/water interface pushes the NPs outward. Their balance causes the NPs to be trapped.[17,18,25] The Marangoni flow at the bubble surface would further drive the trapped NPs to the TPCL. If the bubble is then detached from the surface, the trapped NPs are deposited on the surface as a ring, and this is the mechanism of TPCL deposition using a steady state photothermal surface bubble.[18,19,25,31]

However, in our experiment, we do not wait for the bubble to detach, but instead, we turn off the laser irradiation after the bubble reaches a certain size. With the heat supply absent, the bubble, substrate and the surrounding liquid cool down, and thus the bubble start to shrink (Figure 1c). After the bubble eventually vanishes, a highly concentrated island with closely packed NPs is deposited on the surface (Figure 1d). To further elucidate the mechanism behind the SSBD process, we use videography (30 frames per sec) to characterize the whole bubble shrinking process (**Figure 2**; Movies S1 and S2, Supporting Information). There are two stages in the shrinking of the surface bubble, corresponding to vapor condensation and gas dissolving back to liquid water. The first stage is very fast, on the order of milliseconds.[36,38,39] The second stage, gas molecules dissolving back to water, is found to dominate the shrinking process and
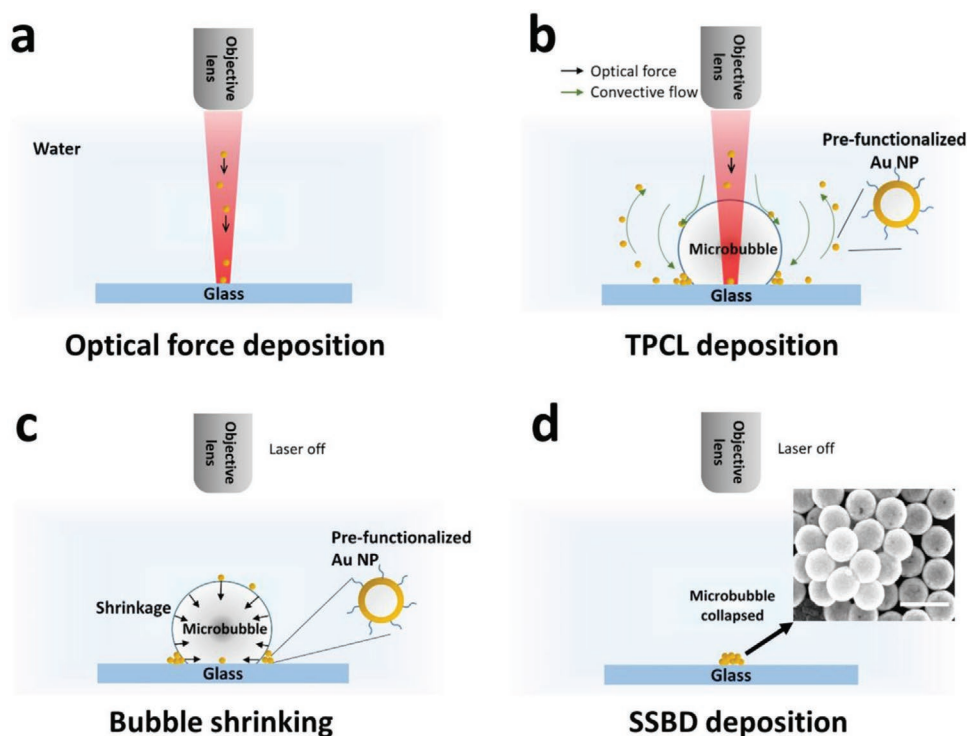
**ADVANCED
SCIENCE NEWS**

www.advancedsciencenews.com

**ADVANCED
MATERIALS
INTERFACES**

www.advmatinterfaces.de

Figure 1. Schematics of a) optical pressure force driving suspended NPs to the surface; b) laser-generated photothermal bubble and the flow surrounding it drives suspended NPs to the three-phase contact line (TPCL); c) laser turned off to allow bubble shrinking which leads to TPCL contraction; and d) concentrated NP island deposited by SSBD due to the complete contraction of TPCL as bubble vanishes. Inset in (d) is a representative scanning electron microscopy image of the SSBD spot (scale bar: 200 nm).

the time scale is on the order of hundreds of seconds, which is consistent to other studies.[39,40] For instance, a bubble of 40 µm in diameter lasts about ~300 s before it eventually vanishes (Figure 2a). An important finding in the second stage is that the bubble shrinkage is accompanied by the contact-line contraction (Figure 2b). Here, we note that the contact line (w) and the radius of surface bubble (a) are independent parameters.[34] This

is believed to be critical to the deposition of highly concentrated NP spots. If the bubble collapses without contact line contraction, the NPs adsorbed on the TPCL should have a ring shape when they are deposited, as found in some other studies.[16] In our case, the deposited site has a filled circular shape.

However, the decrease in contact line width is not continuous. As illustrated schematically in Figure 2b and shown
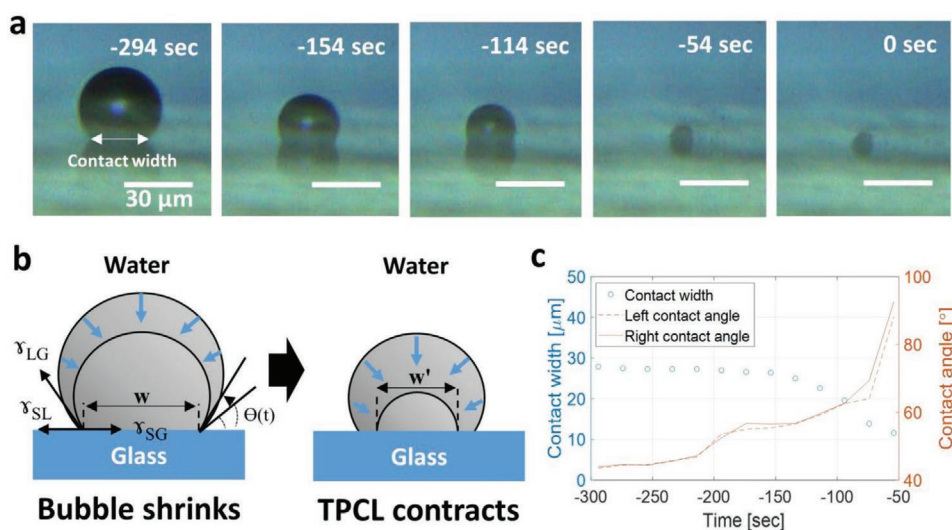

Figure 2. a) Successive optical images from the side view of a typical shrinking bubble on the glass substrate. b) Schematic illustration for of the contact line contraction during bubble shrinkage. c) Contact width and contact angle as a function of time during the bubble shrinking process.

quantitatively in Figure 2c, the bubble initially maintains a nearly constant contact line width while the contact angle increases gradually. When the contact angle reaches a critical value, θ_{cr} (55 ± 1° in our case), the contact line width starts to decrease rapidly. This phenomenon can be further explained by analyzing the force balance at the TPCL via Young's equation

$$\gamma_{SL} + \gamma_{LG}\cos\theta = \gamma_{SG}, \quad \text{for } \theta \le \theta_{cr} \tag{1}$$

$$\gamma_{SL} + \gamma_{LG}\cos\theta < \gamma_{SG}, \quad \text{for } \theta > \theta_{cr} \tag{2}$$

where γ_{SL}, γ_{LG} and γ_{SG} represent the interface energy of solid-liquid, liquid-gas and solid-gas, respectively (Figure 2c). Due to the tendency to minimize liquid-vapor surface energy, bubble would always like to maintain a spherical shape. When the surface bubble shrinks, the contact line should tend to contract to keep the bubble as spherical as possible. However, the contact line is pinned and thus the bubble becomes increasingly non-spherical (i.e., liquid-gas surface energy, γ_{LG}, increases), which leads the contact angle to increase and the surface tension of bubble to build up (Equation 1). This continues until the contact line can no longer be pinned by the pinning forces, which eventually leads to the contraction of the contact line (Equation 2). As shown in Equation 2, when the contact angle is larger than the critical angle on the hydrophilic substrate, γ_{SG} becomes dominant. This leads to the contraction of the contact line (Figure 2b) and the NPs adsorbed on the TPCL are pulled inward.

2.2. Demonstration of the Biocompatibility of SSBD

The above understood mechanism suggests that the NPs captured by the TCPL can be piled into a concentrated spot as the bubble shrinks to vanish and the whole process happens without laser heating. This would maintain the viability of the molecules attached to the NPs. We demonstrate the potential applicability of this SSBD technique for bio-sensing applications by directly depositing single-stranded DNA (ssDNA)-functionalized core-shell AuNPs onto a bare glass substrate.

NPs made of a silica-core (≈100 nm in diameter) and a Au-shell (≈10 nm in thickness) are used since they have a SPR peak (≈785 nm) matching the wavelength of our excitation laser (Figure S2, Supporting Information). The ssDNA is conjugated to the AuNP surface through the gold-sulfur bonding chemistry[41] (**Figure 3**a, see the Experimental Section for details). To achieve this bonding, the ssDNA oligonucleotides were custom modified with thiol groups at the 3' end (Integrated DNA Technologies, Inc.), which binds to the gold surface according to the salt aging protocol described by Hurst et al.[42] The ssDNA consists of 35 bases and 57.1% of GC content, and it is capable of
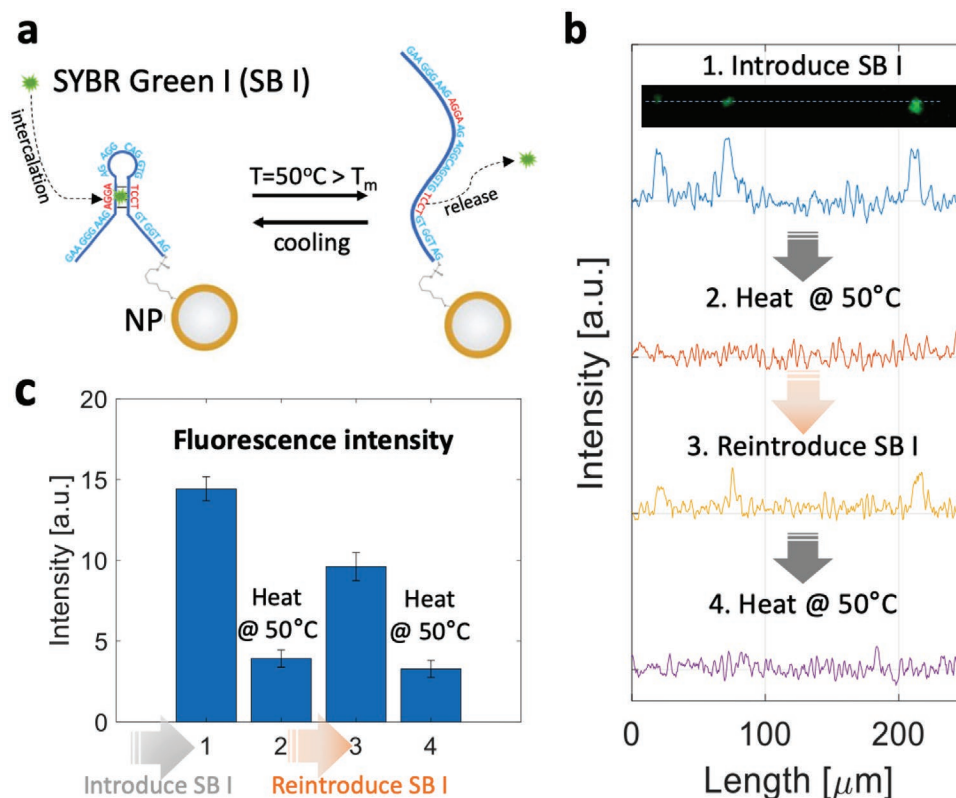

Figure 3. a) Schematics of testing the viability of the ssDNA using its hairpin structure that can use SB I as a reporter. Upon heating, the hairpin structure will open up and the SB I released. b) Line profiles of the fluorescence signals from the SSBD-deposited ssDNA-AuNP islands in two heating cycles, involving four steps: introduction of SG I, release of SG I by heating at 50 °C, reintroduction of SG I, and re-heating. c) Average fluorescence intensities measured from 20 different SSBD-deposited spots, where the error bars represent the standard deviation.

**ADVANCED
SCIENCE NEWS**

www.advancedsciencenews.com

**ADVANCED
MATERIALS
INTERFACES**

www.advmatinterfaces.de

folding so as to form a hairpin loop through complementary hydrogen bonding (Figure 3a).[43] The presence of this secondary structure (i.e., hairpin) at room temperature is beneficial for our detection purpose because it can provide a binding site of intercalating dyes, such as SYBR Green I (SG I), to confer fluorescence emission.[44] SG I (Invitrogen) is a staining dye that specifically binds to double-stranded DNA and emits green fluorescence. The hairpin structure of our ssDNA provides such a binding site (Figure 3a) as predicted using the IDT SciTools.[45] The estimated free energy (ΔG) is −1.75 kcal mol^{-1} and the melting temperature (T_m) is 45.9 °C.[45] Thus, the spontaneous hairpin structures at room temperature should allow us to observe florescence signals with SG I added, if the ssDNA survives the SSBD process. The viability of the ssDNA can be further verified by thermal cycling above the T_m, which will break the complementary hydrogen bonds to release the fluorescent dye that was intercalated at the hairpin loop, leading to a decrease in fluorescence intensity.

As shown in Figure 3b, green fluorescence signals are apparent from the SSBD-deposited NP spots after SG I was introduced to the solution. When the solution is heated to 50 °C, the signals almost disappear, and when cooled down and SG I re-introduced, fluorescence is seen again despite reduced intensity. Figure 3c quantitatively shows the average fluorescence intensity from an array of 20 SSBD-deposited spots, where the error bars are the standard deviation. This results indicate that the signals before and after heating are significantly different. We also note that the intensity decrease in the second thermal cycle (from ≈14.5 to ≈9.5) potentially suggests that the SSBD technique is even less damaging than heating at 50 °C for the biomolecules. These results confirmed that the SSBD process can maintain the viability of the functional molecules on NPs, which makes it a technique compatible to biological applications.

2.3. Comparison with Other Deposition Mechanisms

We further compare the SSBD method to the other two deposition mechanisms mentioned previously (i.e., optical pressure deposition and contact line deposition). In the optical pressure deposition (Figure 1a), the optical force on the NPs drives them to the surface[28] and all deposited NPs have been exposed directly to the laser irradiation. We intentionally reduced the laser power density (≈3.6 mW μm^{-2} at the focal plane) so that no surface bubble is generated within the period of laser irradiation. To produce dense patterns on the glass substrate as shown in **Figure 4**a, the optical shutter is opened and closed for 30 times at the same location, after which a pattern of about ≈15 μm in diameter, similar to the laser diameter (≈12 μm), is produced. Survivability of the biological molecules on the AuNP surfaces after deposition is examined by intercalating dye, but fluorescence signal cannot be detected. This result agrees with our expectation considering that the high absorption cross-section (as shown in Figure S1 in the Supporting Information: ~2.3 × 10^{-14} m^2 for the core-shell AuNPs solution[25,46]) of AuNPs may induce extreme heating of the NPs and even nanocavitation[27,28] when directly irradiated by the laser at the SPR peak. This would inevitably result in the destruction of ssDNA attached on the NP surface.
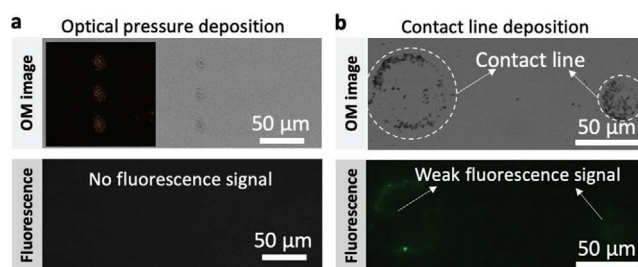

Figure 4. a) Top: Bright and dark field (inset) images of deposited patterns from the optical pressure deposition method (see Figure 1a for schematic). Bottom: No fluorescence signal can be detected from the deposited spots. b) Top: Optical microscope image shows deposited AuNPs from the contact line deposition around a steady state photothermal bubble (see Figure 1b for schematic). Ring-like patterns correspond to the contact line of the thermal bubbles. Bottom: Fluorescence signal is detected using 1s exposure time – the same as that in Figure 3.

The contact line deposition mechanism leverages the fluid flow around the thermal bubble to capture and immobilize suspended particles at the TCPL (Figure 1b).[16–19,31] Although this technique is efficient in trapping NPs, maintaining the bubble with continuous laser heating is not desirable as the bubble area is kept at a relatively high temperature which may lead to degradation of biomolecules. In addition, since the contact ring is usually a few times larger than the laser spot, the concentration of the deposited NPs will be low compared to the SSBD-deposited spots. As shown in Figure 4b, the deposited NP areas are 3–5 times larger than the laser spot size (≈12 μm) depending on the sizes of bubbles when they detach from the surface. As expected, we also see that the patterns of the deposited NPs are close to rings with higher density at the periphery. The fluorescence signal intensity from the deposited NPs (Figure 4b, bottom) is apparently lower than that from the SSBD-deposited spots (Figure 3b), which can be partially attributed to the fact that the contact line deposited NPs spread over a larger area and thus lower density, besides thermal degradation of the bio-molecules.

2.4. Controlling the SSBD Process

The ability to control the SSBD process is critical to its future applications. We believe that the SSBD process can be intensified by the influence of various experimental factors. For example, a lower-temperature bulk fluid may act to enhance the Marangoni flow by causing a larger temperature difference at the bubble boundary,[23,24] and a change in air solubility may affect the bubble size.[39] However, in general, since there is a relationship between temperature and gas solubility in water, careful attention is required to control the deposition of AuNPs by surface bubbles. Thus, we note that the SSBD experiments were performed at room temperature, and waited for a sufficient time until one bubble process was completed to avoid heating of the bulk fluid.

When implementing the SSBD for mass production of sensors, the lifetime of bubble is important because it can be the determining factor of the fabrication time scale. We first study the lifetime of bubbles with different peak sizes, which are achieved
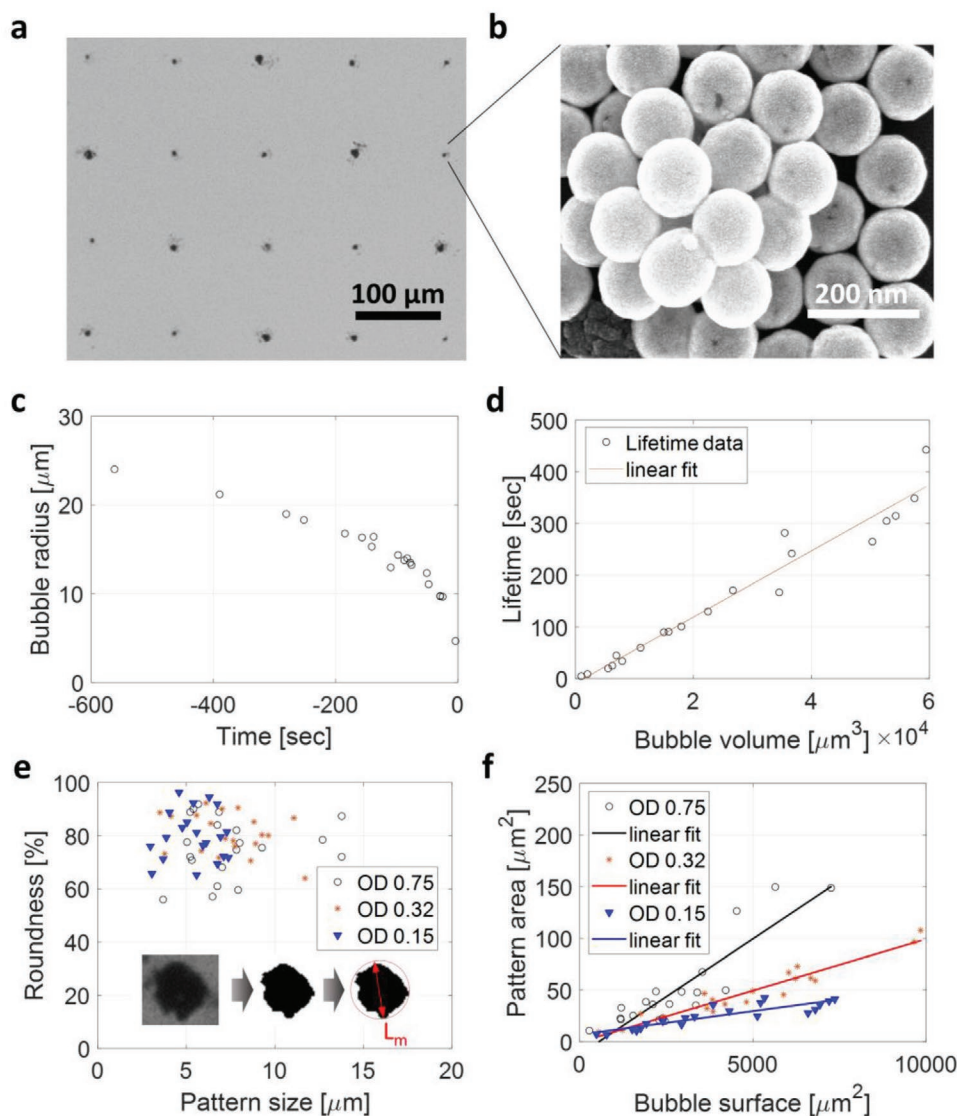
**ADVANCED
SCIENCE NEWS**

www.advancedsciencenews.com

**ADVANCED
MATERIALS
INTERFACES**

www.advmatinterfaces.de

Figure 5. a) An array of 20 micropatterns produced by SSBD using ssDNA-functionalized AuNP suspension with an optical density (OD) of 0.75 at 800 nm. The peak radii of the bubbles are tuned by controlling the laser illumination times (between 1 and 5 sec). b) A typical SEM image of the deposited spot, showing highly concentrated and closely packed NPs. c) A plot of initial radii of bubbles vs. their shrinkage time. d) Lifetimes of bubble as a function of the peak volume. The line fitting indicates that the lifetime shows the power-three dependence. e) Roundness of fabricated patterns as defined in Equation 4. Three different concentrations (OD of 0.75, 0.32, and 0.15 at 800 nm) of prefunctionalized NP solutions are studied. Inset illustrates how the pattern size (L_m) is defined, and the roundness is the ratio between the black area and the area of the peripheric circle (red dashed circle). f) The correlation between surface area of generated bubble and SSBD-deposited pattern area.

by varying the illumination time (1–5 s) of the incident laser. We fabricate a 5×4 microarray of patterns on the glass substrate with the pitch of ≈100 µm (**Figure 5**a). In all cases, the SSBD deposited NPs are dense and closely packed (e.g., Figure 5b). Assuming ideal gas and diffusion-governed process, Baffou et al. reported that the lifetime of a microbubble (τ_B) can be estimated as[40]

$$\tau_B = \frac{P_0 K}{6RTD\gamma} a^3 \qquad (3)$$

where P_0 is ambient pressure, γ (72×10^{-3} N·m^{-1}) is surface tension, K is Henry's coefficient, R is ideal gas constant (8.31 J·mol^{-1}·K^{-1}), T is temperature of the microbubble and D

is diffusion coefficient. Based on our measurements, the lifetime of microbubble estimated from videography scales linearly with the volume (i.e., a^3) of the bubble as shown in Figure 5d, which is consistent with the above equation and previous research.[40] Our results suggest that the SSBD process would have a time scale of seconds to several minutes, depending on the size of the bubble. In mass production, one may generate a large array of bubbles and let them shrink simultaneously to increase productivity.

It is expected that the size of bubble should directly influence the size of the eventually deposited NP spot size. In a similar vein, controlling the concentration of the NPs in the solution provides another route to tune the amount of NPs the bubble

Table 1. Fitting parameters for the surface area of bubble and pattern area shown in Figure .5f

OD at 800 nm	Linear fitting		
	Slope	Intercept	R^2
0.75	0.0224	−12.2	0.789
0.32	0.0100	−0.3	0.926
0.15	0.0045	7.1	0.786

can capture. To analyze the above two controlling strategies, we prepare three different concentrations of functionalized AuNP suspensions, including optical densities (OD) of 0.75, 0.32, and 0.15 at 800 nm. At each concentration, we produce 20 bubbles with different peak sizes. The sizes of the bubbles are determined through videography analysis, and the images of the deposited AuNP patterns are observed using an optical microscope. To define the size of the pattern, roundness (inset in Figure 5e) is first introduced as

$$Roundness\,(\%) = \frac{4 \times A_{Au}}{\pi L_m^2} \tag{4}$$

where A_{Au} is the area of the AuNP pattern, and L_m is the length of the major axis, which is used to denote the pattern size. Figure 5e shows that the patterns all have roundness greater than 50% with a mean value of ≈80% and a spread of ≈20% (see Figure S3 in the Supporting Information for the histogram of roundness). It is also observed that when the NP concentration increases, the average size of the spots increases but the average roundness does not change significantly. Figure 5f shows the pattern area as a function of the calculated surface area of bubble. For each concentration, pattern area and bubble surface area generally follow a linear relation, with the slope of the linear fit increases with the concentration of the NPs. The fitting parameters are shown in **Table 1** for the three linear curves. Larger bubble surfaces can capture more NPs from the suspension, which are eventually brought to the TPCL before it contracts to a concentrated spot upon bubble vanishing. As a result, the SSBD-deposited spot area should scale linearly with the surface area of bubble as observed in Figure 5f. A simple model relating the SSBD spot size, OD and bubble surface area can also be obtained by fitting to all data in Figure 5f, and the model is shown as Equation S1 in the Supporting Information (see Figure S4 in the Supporting Information for the parity plot of predicted pattern area) in the Supporting Information. Such information is useful for the practical control of the spot size of the SSBD process.

3. Conclusion

In summary, we have demonstrated a SSBD technique that can deposit bio-molecule-functionalized NPs directly on substrate for biosensing purposes. The key of the SSBD process is its low temperature feature, which maintains the viability of the bio-molecules. The photo-excited thermal bubble captures NPs in the suspension at the TPCL, and when the laser light is turned off, the shrinking bubble leads to the contraction of the contact line, which pulls the captures NPs to a small spot. Such deposited spots show high concentrations of closely packed NPs. We have also tested the optical pressure deposition technique, but it damages the bio-molecules due to the high temperature of the NPs upon laser excitation. The conventional contact line deposition using a steady state thermal bubble shows much larger deposited rings and weaker biosensing signals compared to those of SSBD. We have also shown that by controlling the bubble size and the NP concentration in suspension, the SSBD spot size can be tuned. We expect the results from this work to provide new opportunities for direct deposition of functionalized NPs which may greatly contribute to the advancement of lab-on-a-chip based biosensors.

4. Experimental Section

Optical Setup for Nanoparticle Deposition: An 800-nm femtosecond pulsed laser (linear polarized Gaussian beam) with a repetition rate of 80.7 MHz and a pulse duration of 200 fs was focused in the prefunctionalized NP suspension using a 20 × objective lens with a numerical aperture of 0.42. 2 mL of functionalized AuNPs was dispersed in the cuvette. The length of the laser beam path in the cuvette was fixed at 4 mm using a PDMS holder. Commercial microscope slide glass (Superfrost Plus Micro Slide, VWR international, LLC.) was used as a substrate for all experiments.

Preparation of Prefunctionalized AuNP: Reduction of thiol-modified DNA was performed using Tris(2-carboxyethyl)phosphine hydrochloride (TCEP) (20×10^{-3} M). Blending DNA with TCEP reduction agent, the solution was incubated at room temperature for 3 h. The cleaved DNA was then purified by a NAP-5 column (illustra NAP Columns, GE Healthcare). The purified DNAs were injected to a core/shell AuNP solution (Auroshell, Nanospectra Biosciences, Inc., number density of 2×10^9 mL^{-1}) containing 0.01 M phosphate buffer (PB) and 0.01% sodium dodecyl sulfate (SDS). The DNA and AuNPs solution was then incubated at room temperature for 20 min. Concentration of sodium chloride (NaCl) in the DNA/AuNPs solution was increased to 0.05 M by adding a NaCl stock solution (2 M). The solution was then sonicated for 10 s and incubated for 20 min at room temperature. This process was repeated until the concentration of salt in the solution reached 1 M. The final solution was stored at room temperature for 30 h. After the incubation step, the suspension containing salt and functionalized AuNPs was centrifuged and the supernatant was removed. The NPs were then resuspended in DI water. A total of five supernatant removals were carried out by repeating the washing process.

Validation Test Using Intercalating Dye: SYBR Green I (10 000 × concentrate in DMSO, Invitrogen) was diluted (1:50) with a phosphate buffered saline (PBS) 1 × solution. The deposited patterns were stained using 100 µL of diluted SYBR solution for 20 min. After washing with PBS 4 × solution and DI water, the patterns were immersed in a 100 µL of PBS 1 × solution. Images were taken by an inverted fluorescence microscope (Eclipse Ti, Nikon). In the validation test, the prewarmed PBS 1 × solution was filled to remove the intercalating die from the DNA and the patterned samples were heated on a hotplate (50 °C) for 15 min.

Supporting Information

Supporting Information is available from the Wiley Online Library or from the author.

Acknowledgements

[1] a) A. R. Parker, H. E. Townley, *Nat. Nanotechnol.* **2007**, *2*, 347; b) W. P. Lustig, S. Mukherjee, N. D. Rudd, A. V. Desai, J. Li, S. K. Ghosh, *Chem. Soc. Rev.* **2017**, *46*, 3242.

[2] W.-L. Ong, S. M. Rupich, D. V. Talapin, A. J. McGaughey, J. A. Malen, *Nat. Mater.* **2013**, *12*, 410.

[3] a) L. Wang, R. Yan, Z. Huo, L. Wang, J. Zeng, J. Bao, X. Wang, Q. Peng, Y. Li, *Angew. Chem., Int. Ed.* **2005**, *44*, 6054; b) P. Tao, G. Ni, C. Song, W. Shang, J. Wu, J. Zhu, G. Chen, T. Deng, *Nat. Energy* **2018**, *3*, 1031; c) Y. Pang, J. Zhang, R. Ma, Z. Qu, E. Lee, T. Luo, *ACS Energy Lett.* **2020**, *5*, 437.

[4] a) W. C. Chan, S. Nie, *Science* **1998**, *281*, 2016; b) S. Park, G. Yossifon, *Nanoscale* **2019**, *11*, 9436.

[5] P. D. Howes, R. Chandrawati, M. M. Stevens, *Science* **2014**, *346*, 1247390.

[6] a) A. R. Clapp, I. L. Medintz, H. Mattoussi, *ChemPhysChem* **2006**, *7*, 47; b) Y.-P. Ho, H. H. Chen, K. W. Leong, T.-H. Wang, *J. Controlled Release* **2006**, *116*, 83.

[7] P. L. Stiles, J. A. Dieringer, N. C. Shah, R. P. Van Duyne, *Annu. Rev. Anal. Chem.* **2008**, *1*, 601.

[8] a) V. Gubala, L. F. Harris, A. J. Ricco, M. X. Tan, D. E. Williams, *Anal. Chem.* **2012**, *84*, 487; b) Y. Yang, S. G. Yoon, C. Shin, H. Jin, W. H. Lee, J. Park, Y. S. Kim, *Nano Energy* **2019**, *57*, 195; c) D. Li, C. Wang, G. Sun, S. Senapati, H.-C. Chang, *Biosens. Bioelectron.* **2017**, *97*, 143.

[9] a) S. Park, J. Lim, Y. E. Pak, S. Moon, Y.-K. Song, *Sensors* **2013**, *13*, 6900; b) P. Wang, M. Xia, O. Liang, K. Sun, A. F. Cipriano, T. Schroeder, H. Liu, Y.-H. Xie, *Anal. Chem.* **2015**, *87*, 10255.

[10] a) A. de la Escosura-Muñiz, A. Merkoçi, *Small* **2011**, *7*, 675; b) I.-H. Chou, M. Benford, H. T. Beier, G. L. Coté, M. Wang, N. Jing, J. Kameoka, T. A. Good, *Nano Lett.* **2008**, *8*, 1729; c) I. Choi, Y. S. Huh, D. Erickson, *Lab Chip* **2011**, *11*, 632.

[11] a) H. Zhang, Y. Yi, C. Zhou, G. Ying, X. Zhou, C. Fu, Y. Zhu, Y. Shen, *RSC Adv.* **2017**, *7*, 52782; b) Y.-Y. Kim, Y. Bang, A.-H. Lee, Y.-K. Song, *ACS Nano* **2019**, *13*, 1183.

[12] E. Rabani, D. R. Reichman, P. L. Geissler, L. E. Brus, *Nature* **2003**, *426*, 271.

[13] F. Kim, S. Kwan, J. Akana, P. Yang, *J. Am. Chem. Soc.* **2001**, *123*, 4360.

[14] Y. Zheng, H. Liu, Y. Wang, C. Zhu, S. Wang, J. Cao, S. Zhu, *Lab Chip* **2011**, *11*, 3816.

[15] a) E. P. Furlani, I. H. Karampelas, Q. Xie, *Lab Chip* **2012**, *12*, 3707; b) Y. Xie, C. Zhao, *Nanoscale* **2017**, *9*, 6622.

[16] S. Fujii, K. Kanaizuka, S. Toyabe, K. Kobayashi, E. Muneyuki, M.-a. Haga, *Langmuir* **2011**, *27*, 8605.

[17] C. Zhao, Y. Xie, Z. Mao, Y. Zhao, J. Rufo, S. Yang, F. Guo, J. D. Mai, T. J. Huang, *Lab Chip* **2014**, *14*, 384.

[18] L. Lin, X. Peng, Z. Mao, W. Li, M. N. Yogeesh, B. B. Rajeeva, E. P. Perillo, A. K. Dunn, D. Akinwande, Y. Zheng, *Nano Lett.* **2016**, *16*, 701.

[19] Z. Kang, J. Chen, H.-P. Ho, *Nanoscale* **2016**, *8*, 10266.

[20] N. Armon, E. Greenberg, M. Layani, Y. S. Rosen, S. Magdassi, H. Shpaisman, *ACS Appl. Mater. Interfaces* **2017**, *9*, 44214.

[21] a) G. Baffou, P. Berto, E. Bermúdez Ureña, R. Quidant, S. Monneret, J. Polleux, H. Rigneault, *ACS Nano* **2013**, *7*, 6478; b) S. V. Boriskina, H. Ghasemi, G. Chen, *Mater. Today* **2013**, *16*, 375.

[22] F. Korte, J. Koch, B. Chichkov, *Appl. Phys. A* **2004**, *79*, 879.

[23] K. Namura, K. Nakajima, K. Kimura, M. Suzuki, *Appl. Phys. Lett.* **2015**, *106*, 043101.

[24] K. Namura, K. Nakajima, M. Suzuki, *Sci. Rep.* **2017**, *7*, 45776.

[25] Q. Zhang, Y. Pang, J. Schiffbauer, A. Jemcov, H.-C. Chang, E. Lee, T. Luo, *ACS Appl. Mater. Interfaces* **2019**, *11*, 48525.

[26] a) M. Hu, H. Petrova, G. V. Hartland, *Chem. Phys. Lett.* **2004**, *391*, 220; b) D. Lapotko, *Nanomedicine* **2009**, *4*, 813; c) E. Y. Lukianova-Hleb, A. N. Volkov, D. O. Lapotko, *Langmuir* **2014**, *30*, 7425; d) X. Fu, B. Chen, J. Tang, A. H. Zewail, *Sci. Adv.* **2017**, *3*, e1701160.

[27] E. t. Boulais, R. m. Lachaine, M. Meunier, *Nano Lett.* **2012**, *12*, 4763.

[28] E. Lee, D. Huang, T. Luo, *Nat. Commun.* **2020**, *11*, 2404.

[29] S. Fujii, K. Kobayashi, K. Kanaizuka, T. Okamoto, S. Toyabe, E. Muneyuki, M.-a. Haga, *Chem. Lett.* **2010**, *39*, 92.

[30] B. Roy, M. Arya, P. Thomas, J. K. Jürgschat, K. Venkata Rao, A. Banerjee, C. Malla Reddy, S. Roy, *Langmuir* **2013**, *29*, 14733.

[31] Y. Yamamoto, E. Shimizu, Y. Nishimura, T. Iida, S. Tokonami, *Opt. Mater. Express* **2016**, *6*, 1280.

[32] Y. Yamamoto, S. Tokonami, T. Iida, *ACS Appl. Bio Mater.* **2019**, *2*, 1561.

[33] a) Y. Nishimura, K. Nishida, Y. Yamamoto, S. Ito, S. Tokonami, T. Iida, *J. Phys. Chem. C* **2014**, *118*, 18799; b) K. Namura, S. Imafuku, S. Kumar, K. Nakajima, M. Sakakura, M. Suzuki, *Sci. Rep.* **2019**, *9*, 4770; c) K. Setoura, S. Ito, H. Miyasaka, *Nanoscale* **2017**, *9*, 719; d) T. Uwada, S. Fujii, T. Sugiyama, A. Usman, A. Miura, H. Masuhara, K. Kanaizuka, M.-a. Haga, *ACS Appl. Mater. Interfaces* **2012**, *4*, 1158.

[34] Y. Wang, M. E. Zaytsev, H. L. The, J. C. Eijkel, H. J. Zandvliet, X. Zhang, D. Lohse, *ACS Nano* **2017**, *11*, 2045.

[35] S. Baral, A. J. Green, M. Y. Livshits, A. O. Govorov, H. H. Richardson, *ACS Nano* **2014**, *8*, 1439.

[36] Q. Zhang, R. D. Neal, D. Huang, S. Neretina, E. Lee, T. Luo, *arXiv preprint arXiv:1912.11097* **2019**.

[37] D. Baigl, *Lab Chip* **2012**, *12*, 3637.

[38] Y. Hao, Y. Zhang, A. Prosperetti, *Phys. Rev. Fluids* **2017**, *2*, 034303.

[39] M. E. Zaytsev, Y. Wang, Y. Zhang, G. Lajoinie, X. Zhang, A. Prosperetti, H. J. Zandvliet, D. Lohse, *J. Phys. Chem. C* **2020**, *124*, 5861.

[40] G. Baffou, J. Polleux, H. Rigneault, S. Monneret, *J. Phys. Chem. C* **2014**, *118*, 4890.

[41] J. J. Storhoff, R. Elghanian, R. C. Mucic, C. A. Mirkin, R. L. Letsinger, *J. Am. Chem. Soc.* **1998**, *120*, 1959.

[42] S. J. Hurst, A. K. Lytton-Jean, C. A. Mirkin, *Anal. Chem.* **2006**, *78*, 8313.

[43] A. Jonstrup, J. Fredsøe, A. Andersen, *Sensors* **2013**, *13*, 5937.

[44] J. Huang, X. Su, Z. Li, *Sens. Actuators, B* **2014**, *200*, 117.

[45] R. Owczarzy, A. V. Tataurov, Y. Wu, J. A. Manthey, K. A. McQuisten, H. G. Almabrazi, K. F. Pedersen, Y. Lin, J. Garretson, N. O. McEntaggart, *Nucleic Acids Res.* **2008**, *36*, W163.

[46] Z. Qin, J. C. Bischof, *Chem. Soc. Rev.* **2012**, *41*, 1191.